RESEARCH ARTICLE

PIV measurement inside single and double droplet interaction on a solid surface

Ahmet Gultekin[1,2] · Nejdet Erkan[2] · Uner Colak[1] · Shunichi Suzuki[2]

Abstract

In this study, the spreading velocities within the droplet impact on a sapphire glass surface is investigated with the aid of particle image velocimetry (PIV) method. Experiments are performed for unheated and heated surfaces and droplets with impact velocities ranging from 1.12 to 2.40 m/s which correspond to Weber numbers in the range 40–190. It was observed that the radial velocity is linear throughout a relatively large range of spreading radius. However, the velocity profiles show a non-linear shape outside radial positions owing to the capillary and viscous forces over time. For high-Weber numbers, the linearity of radial velocity profile is more evident due to the viscosity effects in the lamella which are insignificantly relative to the inertia forces. Also, the spreading velocities within the droplet pair are investigated at room temperature using the same methods. Another stagnation point formation was observed in the interaction area. In the last part, radial velocity measurements within the liquid lamellas were compared with analytical and computational models for the temperature of unheated surface. For high-Weber case, the analytical model quite agrees with the linear parts of the radial velocity profiles in the interior radial positions. For moderate Weber case, the predicted radial velocity profile only agrees well with the linear parts of experimental data during early spreading process, but the inconsistency between the analytical model and PIV results rises in the later spreading and receding phases. Comparing the results with the computational simulation show that there is a good agreement for both linear and non-linear parts in radial velocity profiles.

Graphic abstract
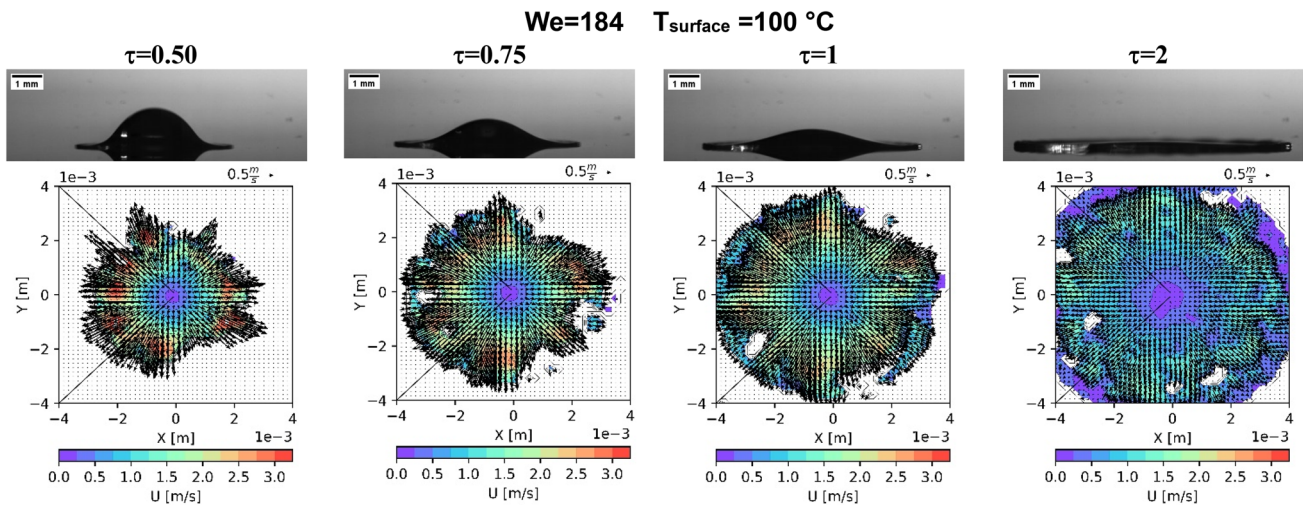
List of symbols

c Constant non-dimensional parameter
D_o Initial droplet diameter (mm)
D_s Spreading diameter (mm)
D Non-dimensional spreading diameter

✉ Ahmet Gultekin
ahmetgultekin@itu.edu.tr

Extended author information available on the last page of the article

d_{h}	Horizontal distance (mm)
$\bar{d}_{\mathrm{h}}$	Non-dimensional horizontal distance
d_{v}	Vertical distance (mm)
$\bar{d}_{\mathrm{v}}$	Non-dimensional vertical distance
E	Energy
h_{l}	Thickness of lamella (mm)
$\bar{h}_{\mathrm{l}}$	Non-dimensional thickness of lamella
q''	Heat flux (W/m^2)
R	Radius (mm)
$\bar{r}$	Non-dimensional radius
T	Temperature (°C)
t	Time (s)
U	Velocity (m/s)
U_{o}	Initial velocity (m/s)
$\bar{u}$	Non-dimensional velocity
Re	Reynolds number
We	Weber number

Greek letters

α	Volume fraction
μ	Dynamic viscosity (Ns/m^2)
ρ	Density (kg/m^3)
σ	Surface tension (N/m)
τ	Non-dimensional time
κ	Mean curvature of the interface
θ	Contact angle
η	Constant non-dimensional parameter

Subscripts

l	Lamella
r	Rim
s	Surface

1 Introduction

The phenomenon of droplet impact onto solid surface can be seen in many industrial applications such as fuel injection in internal-combustion engines (Panão and Moreira 2005), inkjet printing (de Gans et al. 2004), spray coating (Eslamian and Soltani-kordshuli 2017), and spray cooling systems (Kim 2007; Zhang et al. 2013; Cheng et al. 2016). When a droplet impacts onto a surface, different droplet impact dynamics such as splashing, spreading, receding, bouncing can be seen, and these dynamics are discussed in a comprehensive review (Yarin 2006). Rioboo et al. (2002) have investigated time evolution of droplet spreading factor on dry solid surface. They have classified the time evolution of droplet spreading factor into four different phases: kinematic, spreading, relaxation, and a wetting. Droplet impingement onto a heated surface includes a wide range of dynamic processes like kinetic energy conversion, and heat and mass transfer; these are important mechanisms, which occur in a very short time, for understanding the physics of droplet

and surface interactions (Jung et al. 2016). Using different nano-textured surfaces, cooling performance is achieved up to 1 kW/cm^2 (Sinha-Ray et al. 2011; Sahu et al. 2012). Many investigations have been performed about droplet impact onto dry surface or thin liquid film as reported found in a comprehensive review article (Liang and Mudawar 2017).

In the literature, experiments have concentrated more on single droplets, while those regarding multi-droplet interactions are very limited. Coalescence of droplet pair for sessile droplets is investigated in several studies (Menchaca-Rocha et al. 2001; Aarts et al. 2005; Ristenpart et al. 2006; Narhe et al. 2008; Lee et al. 2012, 2013; An et al. 2017). Also, there are limited investigations for multiple-droplet impact with high inertia (Roisman and Tropea 2002; Cossali et al. 2003; Liang et al. 2019; Ersoy and Eslamian 2020). Roisman and Tropea (2002) have studied the impact of droplet pairs on isothermal surfaces experimentally. They have established an empirical model to explain the uprising sheet owing to the interaction of droplet pairs. Liang et al. (2019) examined the droplet pair experimentally at room temperature for simultaneous and non-simultaneous cases. They have classified non-simultaneous events into three main subcases according to the interaction forms. They also emphasized that increasing vertical spacing reduces spreading area and uprising sheet height due to the increased viscous dissipation. Ersoy and Eslamian (2020) experimentally examined uprising sheet evolution with time for simultaneous droplet pairs with large Weber numbers on dry and wet surfaces utilizing liquids with various colors. They found three different uprising sheet types for droplet pair impingement on dry surface.

However, majority of these studies could have provided restricted quantitative data such as the spreading droplet diameter and spreading lamella height. Recent advances in the visualization and imaging technology make the significant progress in the measurement methods. Spreading process after droplet impact is characterized by quick energy transformations and dissipations within a millimeter-scale area. The main limitation is the difficulty of optically accessing to the target area for non-invasive measurements of physical quantity. In such cases, the success of particle image velocity (PIV) measurement is particularly remarkable. PIV measurement method is a flow visualization method used to investigate the behavior of flow in a given region (Adrian 2005). This method allows for more in-depth analysis of dynamic behaviors over time and animation of the flow. Using the PIV method, velocity components in the desired area can be measured. Adequate illumination and high magnification are often essential to obtain good quality data. Nevertheless, increasing the magnification value reduces the visual field and limits the spatial resolution.

Currently, there are limited efforts to use PIV method with droplet interactions in the literature. Most of these

studies have focused on sessile droplets (Kang et al. 2013; Frommhold et al. 2015; He and Qiu 2016; Morozov et al. 2018; Al-Sharafi and Yilbas 2019), or droplet with low We number impact on cold (Karlsson et al. 2019), unheated (Erkan and Okamoto 2014), and heated surfaces (Erkan 2019). Moreover, those concerning droplets with higher We number (Smith and Bertola 2011) impact onto heated surface are quite sparse (Lastakowski et al. 2014). Morozov et al. (2018) experimentally investigated the velocity distribution inside a sessile droplet on a heated surface when a cold droplet falls on the sessile droplet. The results show that, instantly, the interaction between droplets increases the average velocity in the droplet. Erkan and Okamoto (2014) examined the spreading velocities within a single droplet with low We number impinging on a non-heated glass surface in early spreading phase for different impact velocities using PIV method. They indicated that instant radial velocity distributions show linear and non-linear behaviors. The non-linear part is because of the eddy flows created at the external regions of the liquid lamella. Also, Erkan (2019) examined the radial velocity distributions inside a single droplet with low We number impinging on heated surface. PIV measurements of the radial velocity inside the liquid lamella on the unheated surface were compared with a numerical volume of fluid (VOF) model and an analytical model. It was indicated that numerical model can estimate pretty much the velocity profiles. Despite these efforts, there are not enough investigations about the spreading velocities within the inertia-dominated droplet impact on a heated surface.

In this paper, we studied the spreading velocities within the inertia-dominated droplet impact on a heated surface with the aid of time-resolved PIV and shadowgraph techniques. The experiments are performed for droplets with the velocities of 1.12–2.40 m/s corresponding Weber numbers ($We = \rho U_{\mathrm{o}}^2 D_{\mathrm{o}}/\sigma$) varied from 40 to 190, where ρ is the liquid density, U_{o} is the droplet impact velocity, D_o is the initial droplet diameter, and σ is the surface tension of fluid until it is completely disc-shaped ($\tau = \frac{tU_{\mathrm{o}}}{D_{\mathrm{o}}} = 2$, where t, D_{o}, and U_{o} denote physical time, initial droplet diameter and droplet velocity, respectively). Droplets with a Weber number $40 < We < 100$ and $100 \leq We$ are defined as moderate- and high-Weber numbers in this study, respectively. In addition, the spreading velocities within the droplet pair are investigated at room temperature for moderate We cases using the same methods. In addition, radial velocity measurements within the liquid lamellas compared with an analytical model and a computational simulation for unheated surface temperature. Computational simulations are carried out using Star-CCM+, for interface tracking, the volume of fluid model is used. The results provide additional quantitative data to validate new numerical models.

2 Experimental setup

The schematic representation of the experimental setup used in PIV experiments is given in Fig. 1. The main elements of the PIV system are fast camera and laser generator. The laser generator used in this study for droplet illumination is DPSS 532 nm wavelength green laser system with output power 10 W. A set of lenses are arranged to make the planar laser light layer. The light layer is placed in parallel with the sapphire glass. Fastcam Mini camera is equipped with a long-distance microscopic lens which is placed parallel to the laser-lit surface and captures the movement of particles from the bottom through a 2-cm-diameter circular hole. A long-pass filter that cuts wavelengths shorter than 600 nm and transmits longer wavelengths is placed in front of the Fastcam Mini camera. Photron Fastcam SA5 synchronized with Fastcam Mini, captured the shadowgraphy images of droplets from the side. Also, an IR long-pass filter (800 nm) is used to get rid of the laser reflections and to transmit just
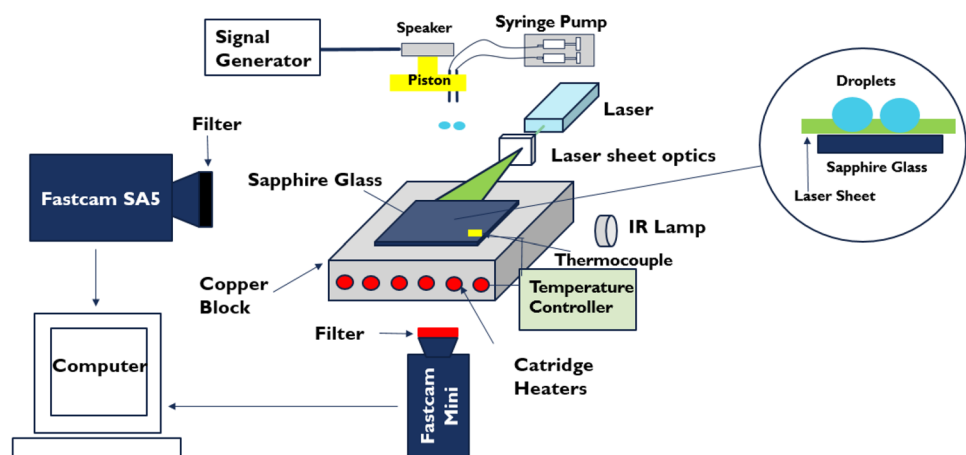

Fig. 1 Schematic diagram of experimental setup for PIV

**Table 1** The impact conditions of single droplets for moderate- and high-Weber cases

Temperature (°C)	Moderate-Weber cases				High-Weber cases			
	D_o (mm)	U_o(m/s)	We	Re	D_o (mm)	U_o(m/s)	We	Re
25	2.42	1.12	42	2710	2.35	2.37	183	5570
100	2.40	1.13	43	2712	2.38	2.36	184	5664
150	2.39	1.12	42	2677	2.38	2.40	190	5712
200	2.38	1.13	42	2689	2.39	2.39	190	5712
250	2.35	1.12	41	2632	2.36	2.37	184	5593

Table 2 The impact conditions of droplet pairs at room temperature

Parameters	Case I		Case II	
Droplet diameter (mm)	2.23	2.25	2.23	2.25
Droplet velocity (m/s)	1.13	1.13	1.50	1.49
We	40	40	70	69
Re	2519	2543	3345	3353
$\overline{d}_h$	1.80		1.76	
$\overline{d}_v$	0.02		0.09	

Fig. 2 PIV images with tracing particle

the IR wavelengths. An infrared lamp source is used in the experiments for the shadowgraph method. From shadowgraph images, droplet impact velocity and initial diameter were determined. Both cameras recorded serial images at 20,000 frames per second. The observation area for PIV camera is 640×480 pixels corresponding to a 0.02 mm/pixel image resolution.

The temperature-controlled test plate system is consisted of a copper block, insulation material, thermocouple, cartridge heaters, temperature controller, and sapphire glass. Twelve cartridge heaters (200 V, 1.25 A 250 W) were installed in the holes on the sides of copper block. The maximum operational temperature is 871 °C for cartridge heaters. The temperature of the heated surface is controlled by a temperature controller integrated with a calibrated K-type thermocouple fixed on the glass using a high temperature band. The maximum absolute uncertainty value for the thermocouple is 1.5 °C. Sapphire glass surface is preferred due to its transparent and high thermal conductivity. The droplet generator was placed vertically up from the surface with a known distance. By shifting this distance, droplet impact velocity can be changed. The impact conditions of droplets [diameter, droplet velocity, center-to-center horizontal spacing (d_h), and vertical spacing (d_v) between droplets] are obtained by pixel analyzing using an open source software (ImageJ) (Schneider et al. 2012) from shadowgraph images and these values are given in Tables 1 and 2 for all cases. Each case was repeated at least three times for the same surface temperature and impact conditions. In this study, distilled water is used in the droplet production. To make the flow visible for velocity measurement using PIV, polymeric fluorescent particles (6 μm) were sufficiently added to
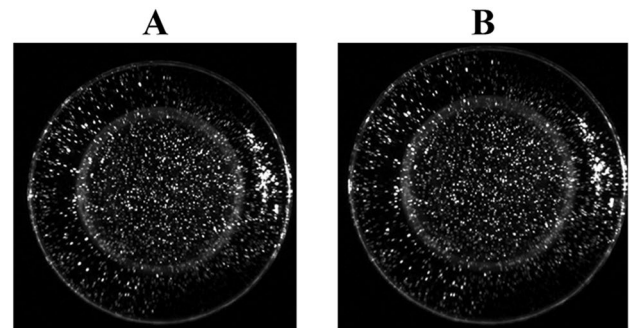
the distilled water as tracer particle. The addition of these particles slightly affects the viscosity and surface tension of pure water (Sakai et al. 2007). Before the experiments, water containing the polymeric fluorescent particles is sonicated around 20 min with an ultrasonic cleaner to distribute the particles in the fluid well.

Sample photo frames obtained from PIV for droplet experiment are given in Fig. 2. The distributions of the particles are clearly visible in the photographs. In PIV analysis, two consecutive photographs (A and B) of the laser-illuminated plane are recorded at t_0 and $t_0 + \Delta t$, respectively. The velocity distribution of the fluid can be found from particle displacement (derived from the distance from which particles travel from A to B) and Δt. With the help of in-house code (Erkan et al. 2008), the velocities of the particles can be easily calculated for a large number of photographs. The laser intensity is 6.5 and the magnification value of the PIV camera is 2. When we increase the magnification value, we can get more clear images. However, increasing the magnification value reduces the visual field and limits the spatial resolution of the measurement. As shown in Fig. 2, there are some dark regions because of insufficient illumination zones on the PIV image. This situation is explained in detail in Ref. (Erkan and Okamoto 2014).

PIV images are divided into interrogation windows. Then, particle displacement is calculated for particle groups by evaluating the cross-correlation of several small query windows. Width and height control the size of the query windows in pixels. Correlation provides the most possible

displacement for a group of particles moving in a straight line between image A and image B. For computing velocity fields, 16×16 pixel interrogation area with a 50% overlapping is used.

3 Results and discussion

3.1 Single droplet case

Figure 3 shows some of the shadowgraph images for droplet at different surface temperatures and selected instants of non-dimensional times. The kinetic energy of the droplet upon impingement is transformed into the liquid's radial motion during the initial stages of contact with the surface. When the droplet expands across the surface, the kinetic energy of

droplet is partly dissipated by the viscous forces. Eventually, when the droplet reaches maximum spreading area, surface tension slows the enlargement by accumulating the residual kinetic energy of the liquid in the interface energy caused by deformation. At this point, droplet changes form into a circular lamella. As expected, for high-Weber cases, spreading area is larger and liquid lamella thinner than the low-Weber cases because of the balance between the impact kinetic energy (E_k) and interfacial energy (E_s) with the dissipated energy by viscosity during spreading process (E_v) and the interfacial energy at the maximum spreading area (E_s'):

$$E_k + E_s = E_s' + E_v. \tag{1}$$

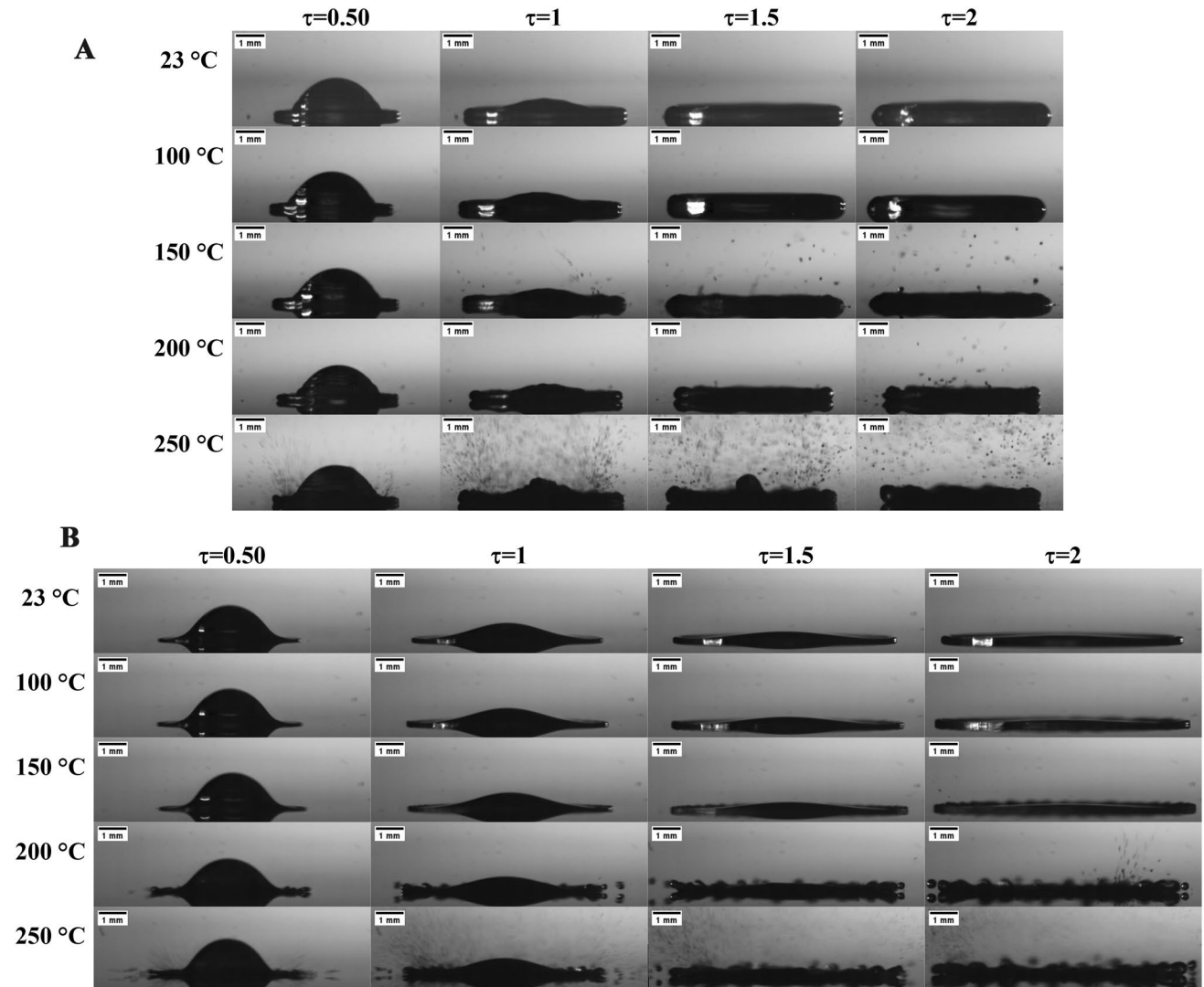At the beginning of spreading process, in droplets impact on the surface up to 200 °C with moderate *We* numbers,

Fig. 3 Shadowgraph images of a droplet impact: **a** moderate- and **b** high-Weber number cases at different surface temperature and non-dimensional times

nucleate boiling and secondary droplets were not observed. Nevertheless, as the liquid lamella approaches its maximum expansion, it was observed that a few small secondary droplets were randomly scattered around due to the growth and explosion of vapor bubbles during the boiling process for 150 °C case. When the surface temperature was 250 °C, a significant number of secondary droplets were observed from the very beginning of the spreading process. The dynamics of vapor bubble growth during spreading are affected by the pressure change throughout droplet impact and by the flow in the lamella. In later stages, the liquid lamella starts to flow radially to the center. For high *We* number cases, finger formations at the rim are observed at 150 °C surface temperature for later stages. These finger formations are strongly dependent on the We and surface temperature. With increasing temperature, fingering pattern occurs earlier because of the viscosity of the liquid decreases with increasing temperature. When the surface temperature were 200 °C and 250 °C, the generation of vapor bubbles occurs at the contact area due to boiling then several tiny secondary droplets occur and scatter around randomly. However, a somewhat higher imbalance was found at bottom interfaces of the droplets, possibly due to intermittent contact with the surface due to higher inertial effects. After some point, this phenomenon causes the liquid lamella smashes into several small parts.

Figures 4 and 5 show the velocity fields for the moderate- and high-*We* cases at 150 °C, the surface temperature. As can be understood from the figures, in the middle region of the vector fields, a stagnation point is developed near the impingement area due to the presence of the solid surface and the lateral outflows. As expected, a larger spreading area occurs in high-Weber number case. As time passes, the velocity magnitudes reduce due to kinetic energy dissipation when the droplet expands. For both cases, droplets are largely in contact with the 150 °C surface. However, growing vapor bubble generation starts on bottom interface and increases with residence time. These bubbles caused random significant disruptions on bottom interface which led to failures in the positions of the tracer particle on the measurement plane. To examine the radial distribution of the velocity, we carried out spatial averages over a quarter field area (Erkan and Okamoto 2014). For this, we choose the areas lightened more uniformly eliminating the dark areas.

Figure 6 shows radial velocity profiles with standard deviations at 150 °C for (a) moderate and (b) high *We* number cases. It was found that radial velocity is linear over a fairly wide range of spreading radius, but owing to the capillary and viscous forces over time, the velocity profiles took on a non-linear form in the external radial positions. Similar behavior is observed and reported in Ref. (Erkan 2016). For high *We* case, the linearity of the radial velocity profile is more apparent because of the viscosity effects in

the lamella relative to the inertia forces which are negligible. Also, radial velocity profiles could possibly be obtained with significantly less volatility owing to less intense boiling which reduced the measurement error compared to the moderate We case. Uncertainty gaps are expanding at external radial locations particularly for the early stage of the spreading process for both cases. The reason is that the gradients of velocity are so large due to the energy loss owing to the viscous dissipation.

In the same way, Fig. 7 shows radial velocity profiles with standard deviations at 250 °C for (a) moderate and (b) high *We* number cases. Radial velocity distribution reveals partly a common pattern in the case of 150 °C surface temperature. For moderate We number case, more bubbles and secondary droplets are observed due to more severe boiling which causes more loss of the tracer particle location. In both cases, higher fluctuations in the radial velocity distribution are found owing to more intense boiling.

Figures 8 and 9 demonstrate the variation of non-dimensional velocity ($\bar{u} = \frac{U}{U_o}$) profiles with spreading non-dimensional radius ($\bar{r} = \frac{R}{D_o}$) for the moderate- and high-Weber number at various surface temperatures. Generally, radial velocities show different profiles at different times after impact owing to the changing relationship of hydrodynamic forces at all surface temperatures. Although the radial velocity is linear over a relatively large range of spreading radius, the velocity profiles took a non-linear shape in the external radial positions due to viscous and capillary forces over time. It can be seen that intense boiling at surface temperature 250 °C, especially in later stages, has a great influence on the radial velocity distribution for moderate We case. For high We case, the radial velocity profile linearity is more evident due to the viscosity effects in the lamella are insignificant relative to the inertia forces at all surface temperatures. It is also observed that the surface temperature does not have a great effect on the radial velocity distribution in the internal radial positions (up to $\bar{r} \approx 0.7$) for high We cases. In addition, the velocity profiles almost show similar trends and values at $\tau = 0.5$ for non-linear parts at all temperatures. Intense boiling at surface temperature 250 °C, especially in later stages, increases the range of radial velocity distribution in external radial locations.

3.2 Droplet pair case

In the areas specified in introduction, the actual process takes place with more than one droplet effect rather than a single-droplet effect. The main difference for the multiple-droplet case is the interaction of nearby droplets. As can be expected, the velocity distribution inside a droplet is significantly affected by the presence of a nearby droplet. To better understand, there is an urgent need to find the gap for
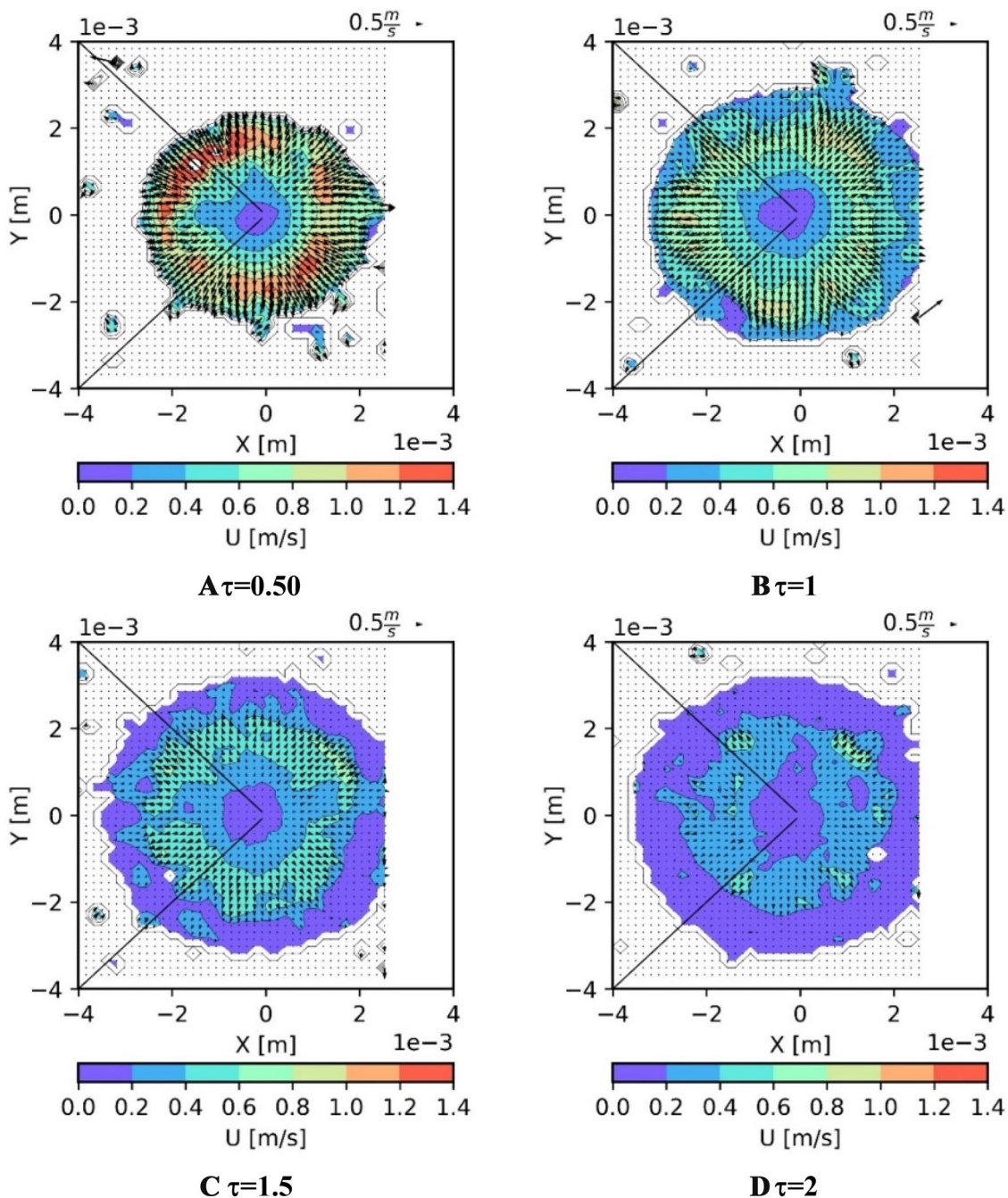
A $\tau=0.50$ **B** $\tau=1$

C $\tau=1.5$ **D** $\tau=2$

Fig. 4 Velocity vector fields at 150 °C and $We=42$ for different non-dimensional times: **a** $\tau=0.50$, **b** $\tau=1$, **c** $\tau=1.5$, and **d** $\tau=2$

the interactions between the droplets. Therefore, we also investigated the spreading velocities within the droplet pair impact onto a sapphire glass surface with the aid of time-resolved PIV and shadowgraph techniques. Experiments are performed for simultaneous droplet pair cases at room temperature. To obtain the synchronous droplet pair, a speaker-connected signal generator has been added to the experimental setup. As the droplets reached a certain size, a 100 kHz frequency and single-mode signal was applied to break the

droplets from the tip of the needles simultaneously. Droplet pair experiments performed only for moderate Weber number case, taking into account the limitations of the current laser power and the maximum possible spatial resolution.

Some of the shadowgraph images for droplet pair at room temperatures and selected instants of non-dimensional times, as shown in Fig. 10, and droplet impact conditions for droplet pairs are given in Table 2. For single-droplet case, a circular liquid lamella develops and extends radially after
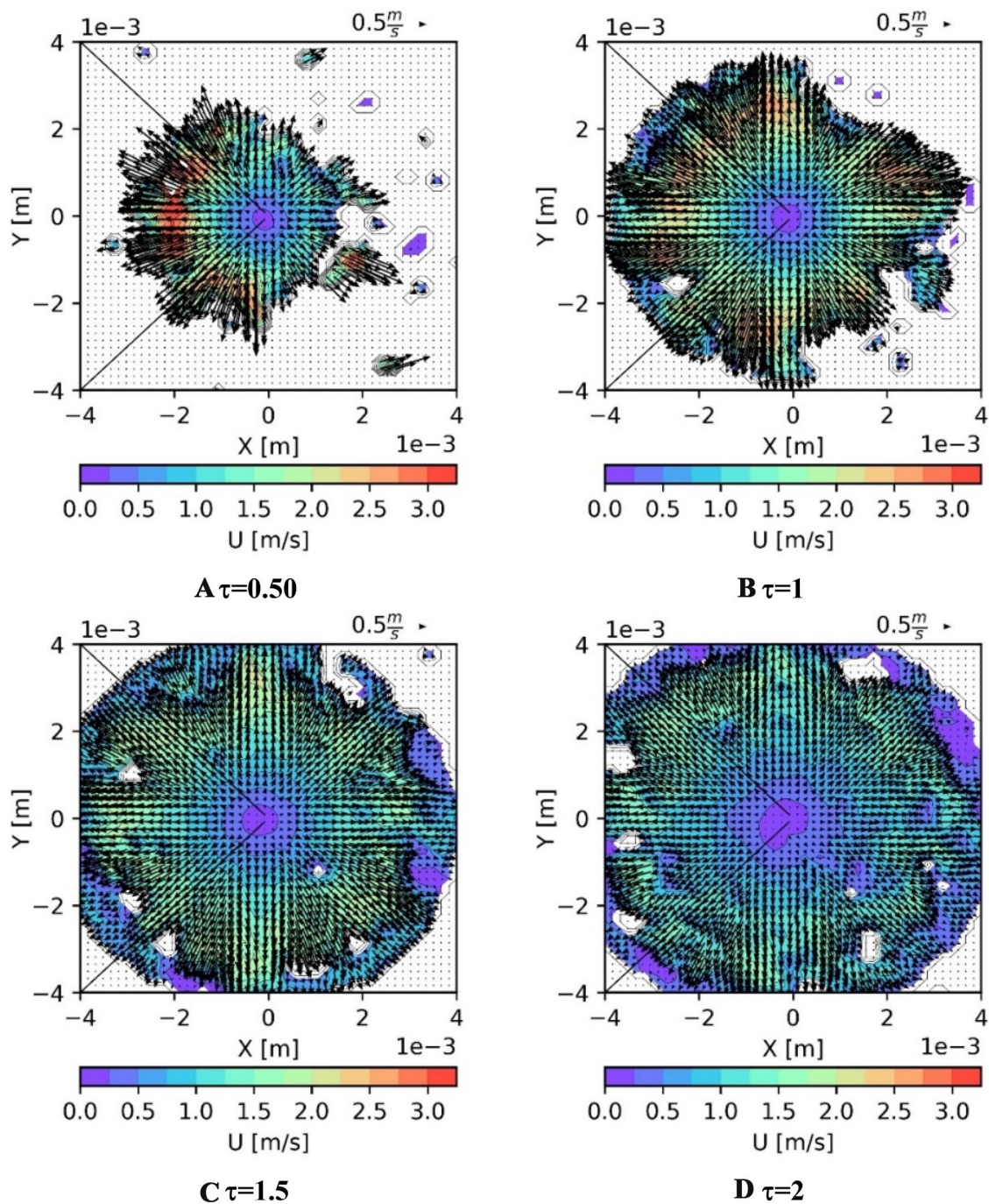
Fig. 5 Velocity vector fields at 150 °C and We = 190 for different non-dimensional times: **a** $\tau = 0.50$, **b** $\tau = 1$, **c** $\tau = 1.5$, and **d** $\tau = 2$

impact on the surface, as shown in Fig. 3. On the other hand, for droplet pair case following impacting surface, droplets spread like a single-droplet case on the sapphire glass after a certain time. Subsequently, the liquid lamellas interact each other at some point (≈ 0.50). This interaction time is highly depend on the horizontal and vertical distance between droplets and impact conditions. The flow activity in the middle areas contributes to a specific phenomenon called uprising

sheet. This uprising sheet formation is a characteristic feature of multiple-droplet interaction and occurs when liquid lamellas have high kinetic energy at the contact point.

Velocity vector fields for simultaneous droplet pair at room temperature for different non-dimensional times as shown in Fig. 11 when Weber number is around 40. As can be seen from the figures, in addition to the middle region of the vector fields, another stagnation point formation was
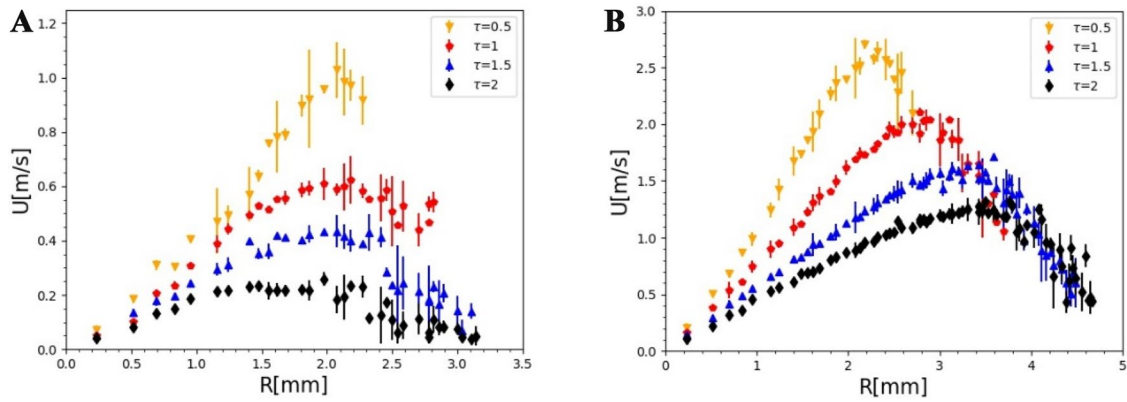
Fig. 6 Radial velocity profiles at 150 °C for **a** moderate and **b** high *We* number cases
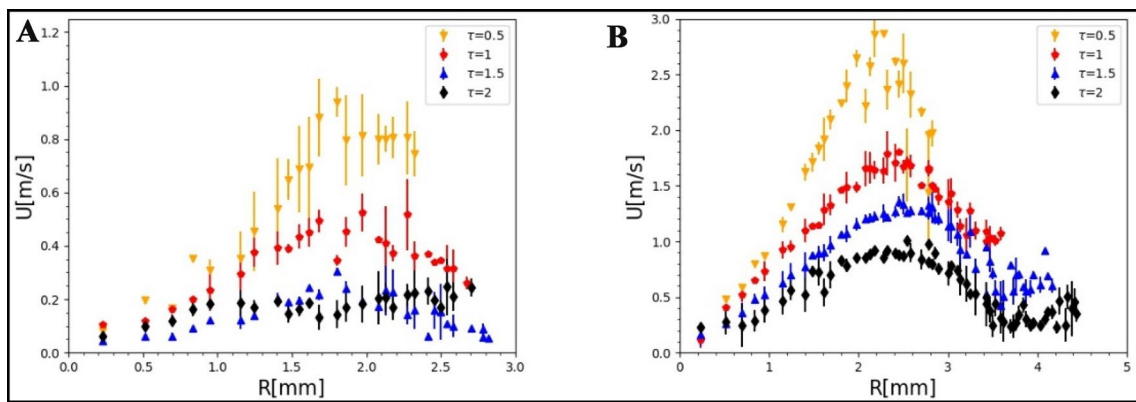

Fig. 7 Radial velocity profiles at 250 °C for **a** moderate and **b** high *We* number cases

observed in the area where the droplets interact. This stagnation point is caused by the upward flow caused by the formation of the uprising sheet. This situation also can be seen from the velocity distribution in the x direction at $y=0$ for different non-dimensional times in Fig. 12 for $We \approx 40$ and $We \approx 70$. Furthermore, when the droplet pair spreads depending on the time, the velocity magnitudes decrease due to the kinetic energy loss due to viscosity.

3.3 Comparison single-droplet case with theory

When a droplet impacts onto surface, it generates a radially expanding flow in lamella (Yarin and Weiss 1995). The lamella is bounded by a rim formed by capillary forces and liquid viscosity stresses. Yarin and Weiss (1995) and Roisman et al. (2002) have proposed the quasi-one-dimensional empirical model for the radial velocity distribution in the lamella, which satisfies equations of mass and momentum balance, for the spreading process in the case of high-Weber number droplet impact:

$$\bar{u} = \frac{\bar{r}}{(\tau + c)} \tag{2}$$

where $\bar{r}$ is non-dimensional radius, and c is an inverse of the initial radial velocity gradient which is determined by using following equations from the initial conditions ($\tau = 1$):

$$3We + 5(1 - \cos\langle\theta\rangle)Re\bar{h}_1 = 10\,Re\,We\bar{h}_1^3 \tag{3}$$

$$c = \frac{\bar{D}_1}{4\sqrt{6}}\left[\frac{1}{12} + \frac{1}{We} - \bar{e}_D - \frac{\bar{D}_1^2}{4We}(1 - \cos\langle\theta\rangle) - \frac{\bar{D}_1\bar{h}_1}{We}\right]^{-\frac{1}{2}} - 1, \tag{4}$$

where $\bar{D}_1$ and $\bar{e}_D$ are represented as:
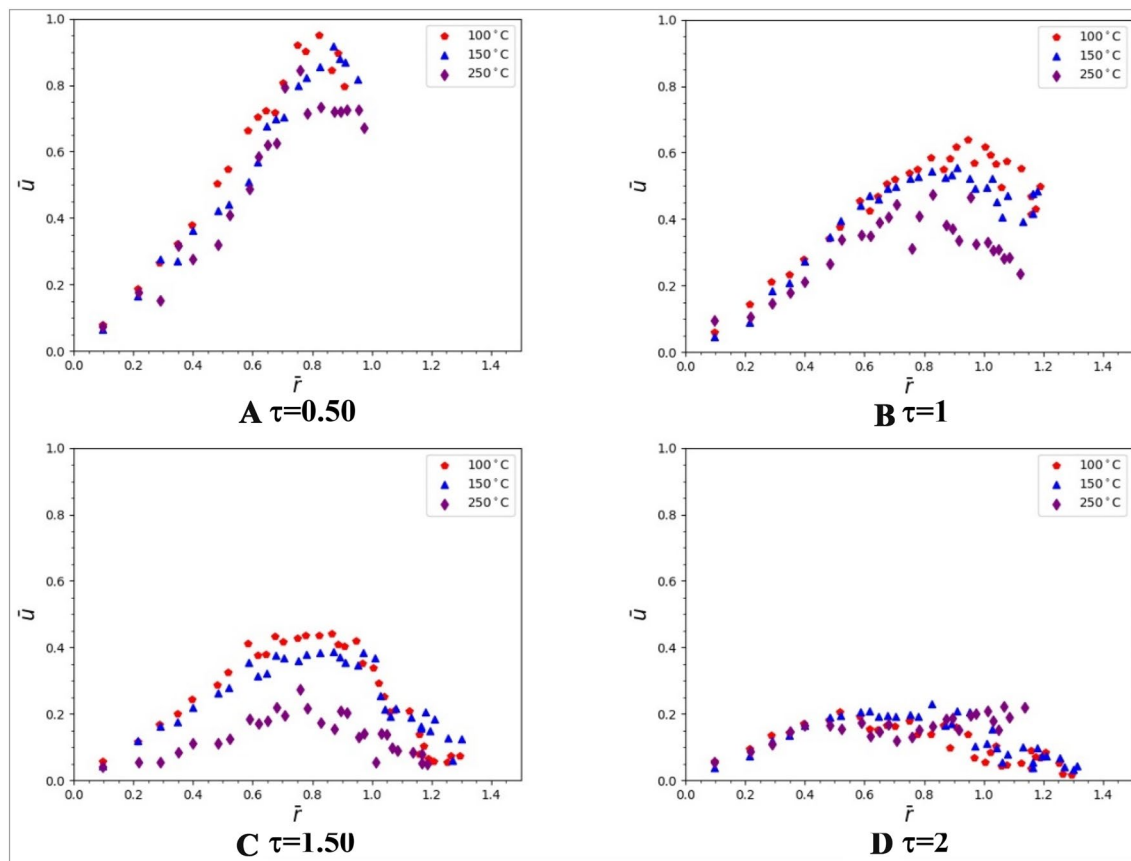
$$\bar{D}_1 = \sqrt{\frac{2}{3h_1}} \tag{5}$$

Fig. 8 Non-dimensional radial velocity profiles obtained from PIV for moderate We numbers: **a** $\tau = 0.50$, **b** $\tau = 1$, **c** $\tau = 1.5$, and **d** $\tau = 2$

$$\bar{e}_{\mathrm{D}} = Re^{-1}\left(\frac{1}{20\bar{h}_1^3} + \frac{3}{5\bar{h}_1}\right). \tag{6}$$

The expression for the radial velocity field in the liquid lamella is valid only for larger times after impingement ($\tau \gg 1$) and the details of the theoretical model are given in their study (Roisman et al. 2002). The constant non-dimensional parameter c values 0.48 and 0.53 are determined from the experimental data with the help of Eqs. (3)–(6) for moderate and high We cases, respectively. The comparison of the PIV results with the analytical model using Eq. (2) at different non-dimensional times for the droplets impact on unheated surface is shown in Fig. 13a for the case of moderate We number. For radius smaller than $\bar{r} \approx 0.9$, all velocity profiles look nearly linear rely on $\bar{r}$ with a time-dependent inclination. The analytical model largely agrees with the linear parts of the velocity profiles during early spreading process up to $\tau \approx 1$. Partial linearity is still observed in the later stages, but radial velocity profiles diverge from the theory. This is most likely due to the direction of the flow shifting towards the center, since the spreading process ends and the recoil process begins. If we multiply radial velocity

profiles with a time delay ($\tau + 0.48$), we can compare all experimental velocity profiles when plotted against $\bar{r}$ with one solid curve, as shown in Fig. 13b.

For high *We* number case, Fig. 14a shows the comparison of the PIV results with the analytical model using Eq. (2) at different non-dimensional times. With radius shorter than $\bar{r} \approx 1.15$, all velocity profiles appear almost linear depending on $\bar{r}$, with a time-dependent inclination. The theoretical model approves generally with the linear parts of the velocity profiles. Contrary to the case of moderate Weber number, the linearity of the radial velocity profile in the internal radial positions is more evident and the agreements govern for a longer period of time due to the viscosity effects relative to the inertia forces are unimportant in the lamella. All experimental velocity profiles are plotted against $\bar{r}$ and compared with one solid curve by multiplying velocity profiles with a time delay ($\tau + 0.53$), as shown in Fig. 14b.

Figure 15a and b shows the comparison of time evolution of non-dimensional radial velocity results with the analytical model using Eq. (2) for different non-dimensional spreading radius for moderate- and high-Weber cases, respectively. Time evolution of radial velocity for the droplets with moderate-Weber number shows good agreements with the theory
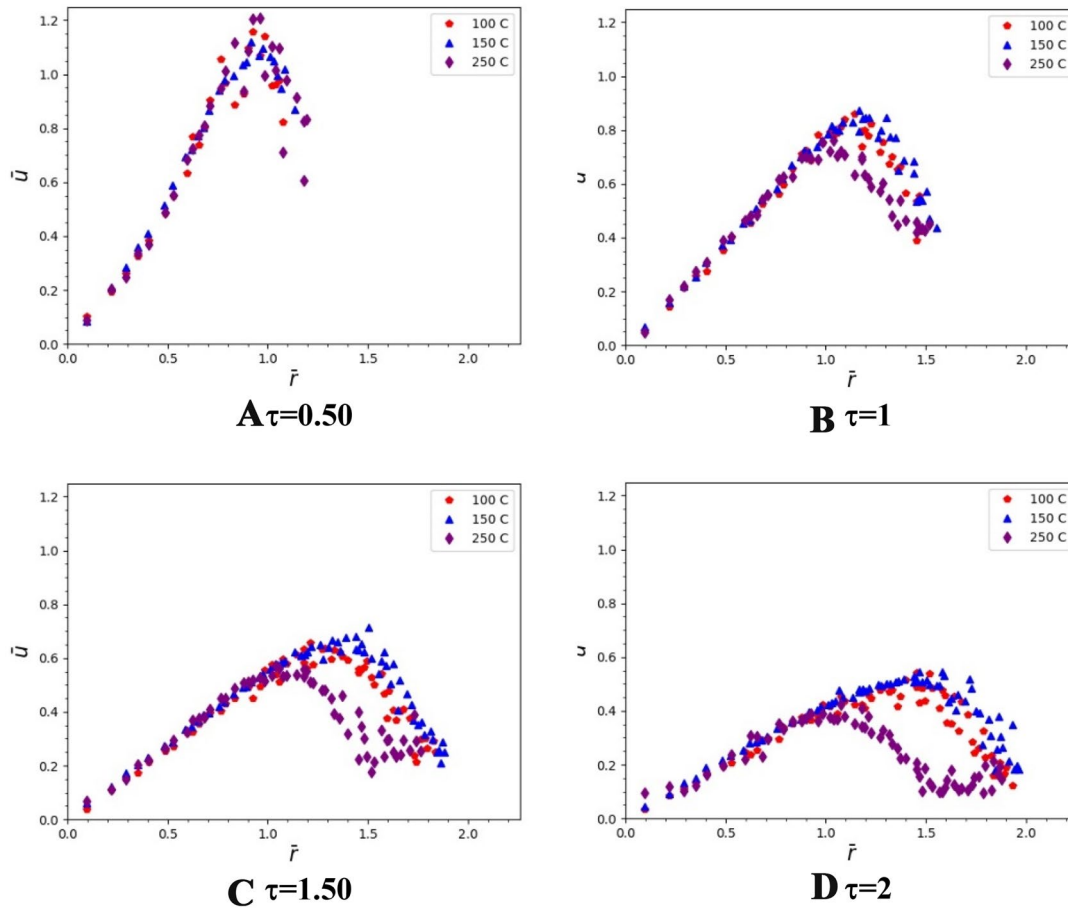
Fig. 9 Non-dimensional radial velocity profiles obtained from PIV for high We numbers: **a** $\tau = 0.50$, **b** $\tau = 1$, **c** $\tau = 1.5$, and **d** $\tau = 2$

at only some certain non-dimensional spreading radius, whereas for high-Weber number case, the agreements are remained for a longer time interval. Analytical model overestimates non-dimensional radial velocity values during early spreading process for both cases. For moderate We number case, with spreading radius shorter than $\bar{r} \approx 0.75$, the theoretical model agrees well generally with the experimental data. However, for $\bar{r} = 1$ case, the analytical model disagrees with the experimental data when non-dimensional time is larger than 1.25 due to the weakening of spreading phase. In other words, wide deviations from the analytical model begin to come out as $\bar{r}$ takes larger values corresponding to the external radial positions. In addition, it was observed that the theoretical model is valid too in the inner radial positions when non-dimensional time is larger than 0.5.

3.4 Comparison with numerical model

Droplet impacts on the surface at room temperature were modeled using the Star-CCM + which is a commercial software package. For interface tracking, the VOF method

proposed by Hirt and Nichols (1981), which is appropriate for the simulation of droplet-surface interaction, is used. In the VOF method, the volume fraction α is defined as:

$$\alpha = \frac{\text{Volume of liquid phase}}{\text{Total volume of the control volume}}, \tag{7}$$

where the α is 1 inside the liquid, 0 in the gas phase, and values between 0 and 1 in the interface area. The difference of VOF in comparison to other methods is that a single momentum equation is solved for the two phases (gas–liquid), where the fluid properties are updated according to the value of volume fraction of the cell. Continuity and momentum equations for gas–liquid are as follows:

$$\nabla \cdot \mathbf{u} = 0 \tag{8}$$

$$\frac{\partial \rho \mathbf{u}}{\partial t} + \nabla \cdot (\rho \mathbf{u} \mathbf{u}) = -\nabla p + \nabla \cdot \mu(\nabla \mathbf{u}) + \mathbf{f}_\sigma + \rho \mathbf{g}, \tag{9}$$

where $\mathbf{g}$ and $\mathbf{f}_\sigma$ are for gravity and surface tension force acting on the fluid at the interface calculated by the continuum
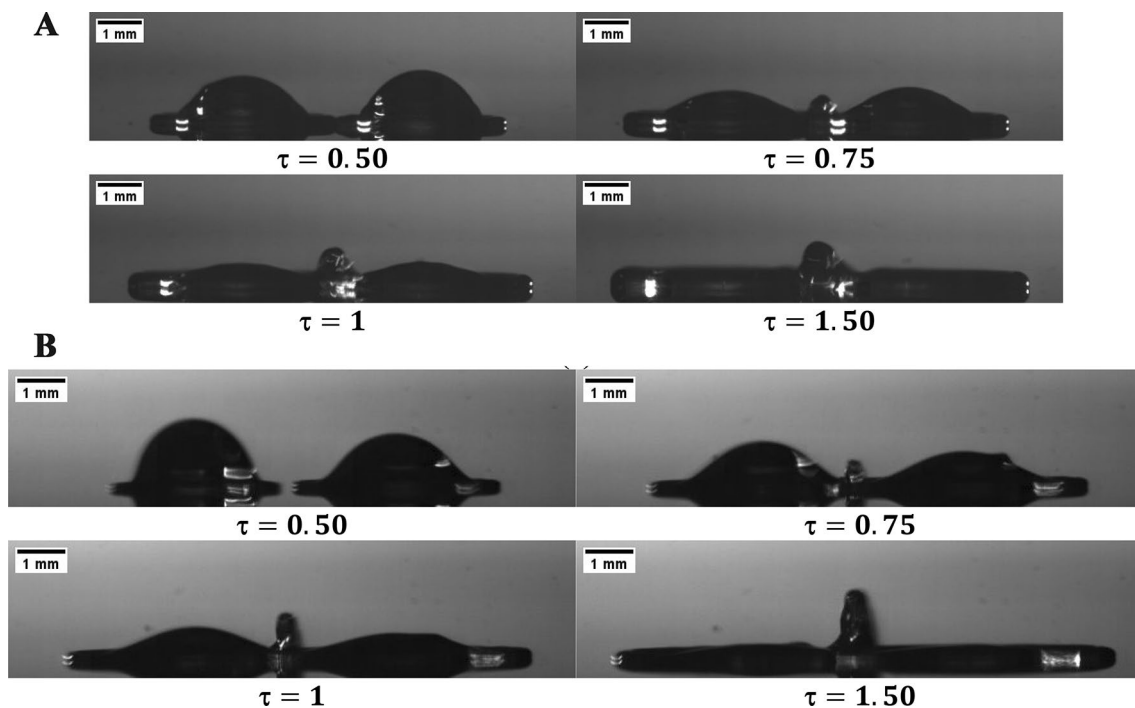
Fig. 10 Shadowgraph images of a simultaneous droplet pair impact on surface at room temperature and non-dimensional times for **a** $We \approx 40$ and **b** $We \approx 70$

surface force model (Brackbill et al. 1992) respectively. In this model, liquid and gases are assumed to be totally immiscible.

$$\mathbf{f}_\sigma = \sigma\kappa\mathbf{n}, \kappa = -\nabla \bullet [\frac{\nabla\alpha}{|\nabla\alpha|}], \mathbf{n} = \nabla\alpha, \tag{10}$$

where κ is the mean curvature of the interface and **n** is the unit vector normal to the interface and directed from liquid to gas. In Eq. (9), the fluid density ρ and viscosity μ are defined by:

$$\rho = \alpha\rho_{liq} + (1-\alpha)\rho_{gas}, \tag{11}$$

$$\mu = \alpha\mu_{liq} + (1-\alpha)\mu_{gas}. \tag{12}$$

A schematic diagram of computational domain with boundary conditions is illustrated in Fig. 16. To minimize simulation work and calculation time, symmetric nature of the problem is considered and symmetry boundary conditions are used. Pressure outlet boundary conditions are applied on top and right sides of the domain, symmetry boundary condition are applied on left side of the domain, also no-slip wall boundary condition with the static contact angle is applied on bottom side of the domain. Quadrilateral mesh is selected for meshing the solution domain and the area near the axis and surface boundary are intensely meshed. The number of total mesh elements is 5×10^5 and

mesh size ranges from 8 to 16 μm. Droplet is defined by field function and placed above the sapphire surface, where the droplet domain was initialized to be liquid and with a respective initial velocity. The velocity of the droplet obtained from shadowgraph images is given to the droplet as the first velocity. Some parameters related to droplet used in the modeling are taken as follows, the density of the water $\rho_w = 998$ kg/m³, the dynamic viscosity $\mu_w = 0.93 \times 10^{-3}$ Ns/m², and surface tension $\sigma = 0.072$ N/m as well as the density of air $\rho_a = 1.225$ kg/m³. The adaptive time step is applied by taking Courant number 0.2 in numerical studies.

Figure 17a, b show the comparison between experimental and computational droplet shapes for both cases at some time steps. Despite some minor differences, the 2-D axisymmetric model is very accurate and there is a good agreement between the numerically predicted droplet shapes and shadowgraph images.

As stated in the introduction, experimental studies do not provide quantitative data to confirm numerical models. The most compared parameters are the variation of the spreading diameter and the height of the spreading droplet. For this purpose, we first verified our model by comparing the variation of non-dimensional spreading diameters with time for both cases, as shown in Fig. 18. As predicted, for high-Weber number cases, spreading area is larger than the moderate Weber number cases, as inertial forces become more significant than surface tension.
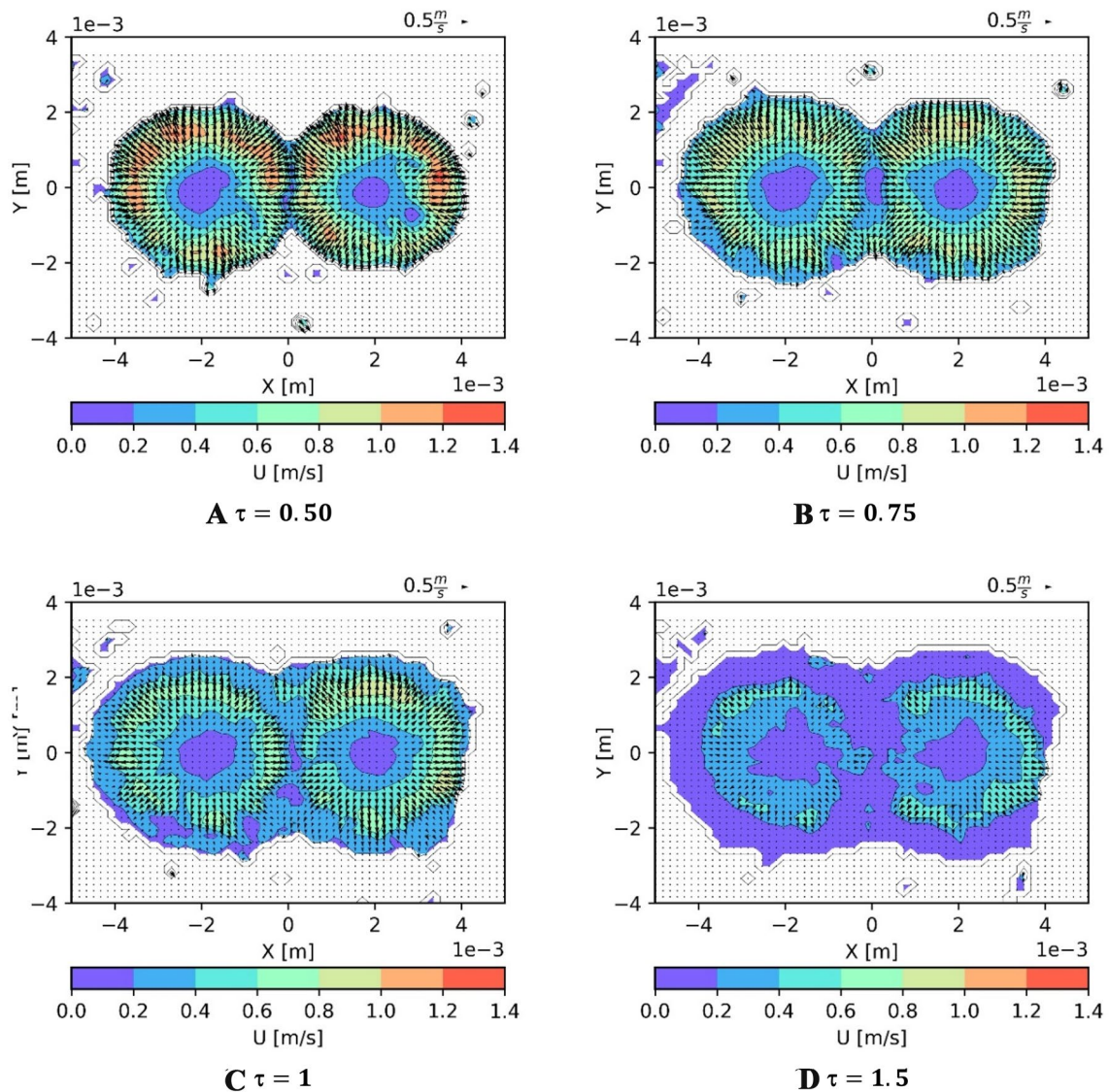
Fig. 11 Velocity vector fields for simultaneous droplet pair at room temperature and $We \approx 40$ for different non-dimensional times: **a** $\tau = 0.50$, **b** $\tau = 0.75$, **c** $\tau = 1$, and **d** $\tau = 1.5$

Experimental and computational radial velocity profiles at room temperature for both cases are given in Fig. 19. The computational results were collected from the surface along a line situated at a height of 0.2 mm. Numerical simulation predicts the instant radial velocity distributions linear and non-linear behaviors very well for both cases. However, for the high *We* case, numerical simulation shows some deviations from PIV results.

4 Conclusion

In this study, we have investigated the radial velocities within the droplets impact on unheated and heated surfaces using PIV and shadowgraph techniques. Unlike previous studies, we have investigated the radial velocities in the liquid lamella until it is completely disc-shaped for moderate- and high-Weber numbers. Using the radial velocity profiles, the variations in the spreading mechanisms were analyzed for both cases. It was observed that the radial velocity is linear throughout relatively large range of spreading radius; however, the velocity profiles took a non-linear shape in the external radial positions owing to the capillary and viscous forces over time for both cases. For high-Weber numbers, the radial velocity profile linearity is more evident due to the viscosity effects in the lamella are insignificant relative to the inertia forces at all surface temperatures. In other words, the surface temperature does not have a great effect on the radial velocity distribution in the internal radial positions. Intense boiling at
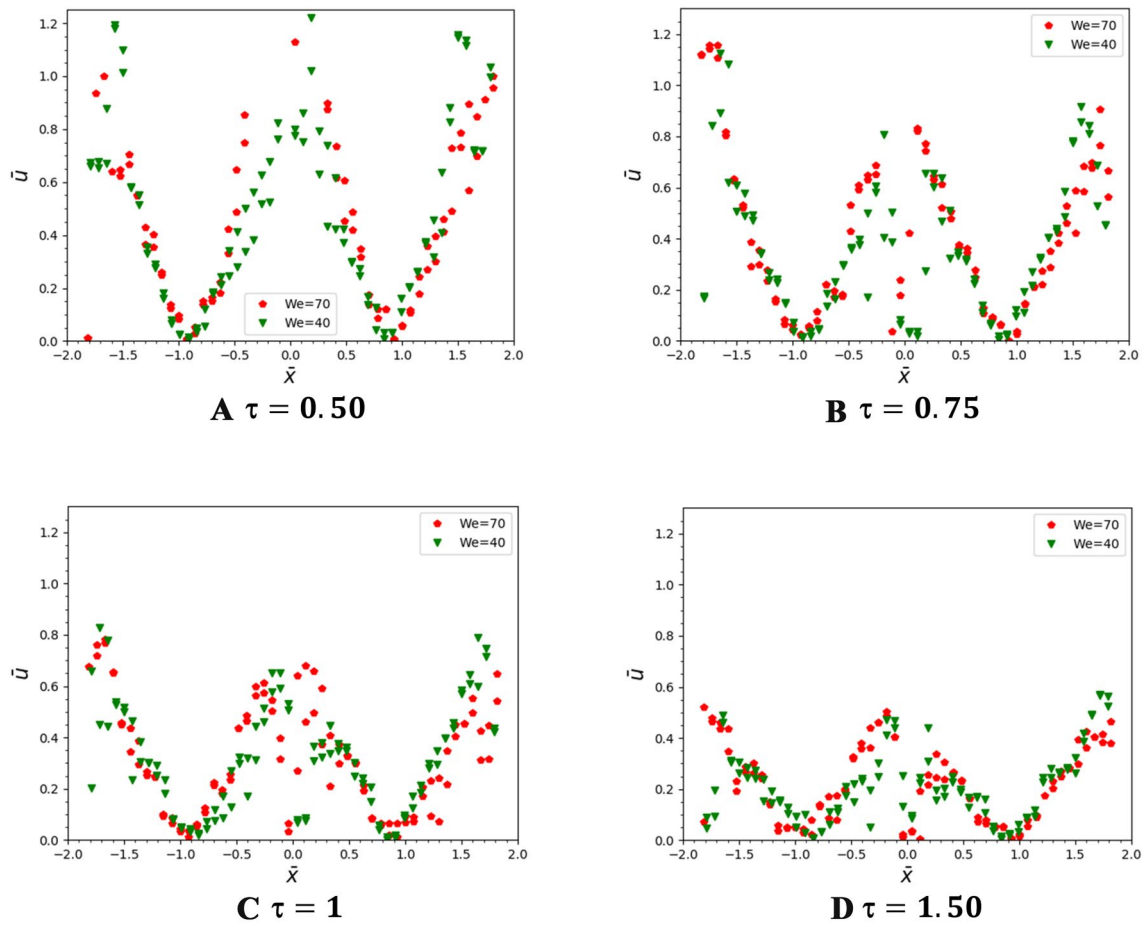
Fig. 12 Non-dimensional velocity distribution in the x direction at $y=0$ when W$e \approx 40$, and $We \approx 70$. for different non-dimensional times: **a** $\tau=0.50$, **b** $\tau=0.75$, **c** $\tau=1$, and **d** $\tau=1.5$
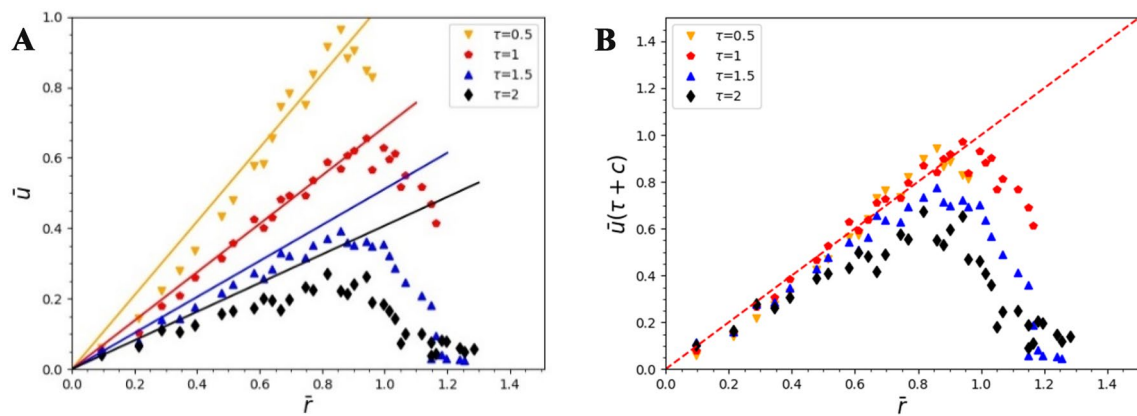

Fig. 13 **a** Non-dimensional radial velocity profiles, symbols represent the PIV results, while the solid curves represent Eq. (2). **b** The variation of normalized velocity $\bar{u}(\tau+0.48)$ with non-dimensional radius at room temperature for moderate We number case
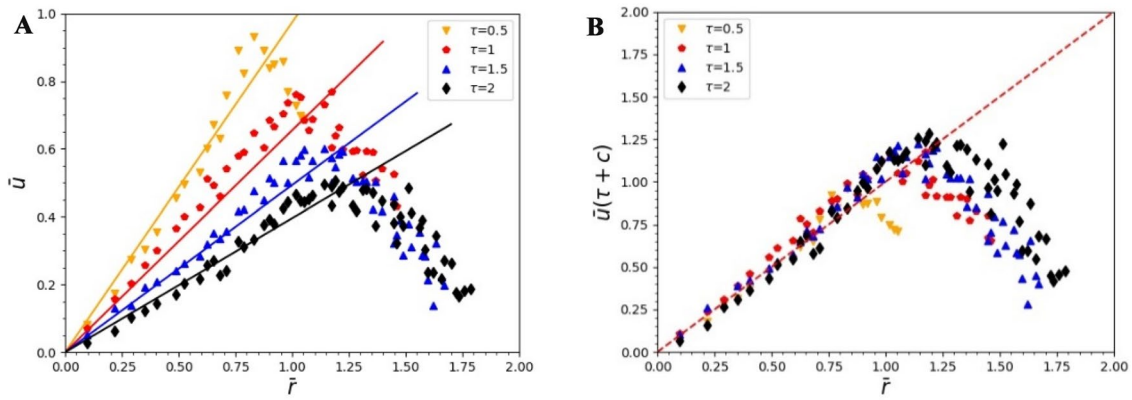
Fig. 14 **a** Non-dimensional radial velocity profiles, symbols represent the PIV results, while the solid curves represent Eq. (2). **b** The variation of normalized velocity $\bar{u}(\tau + 0.53)$ with non-dimensional radius at room temperature for high We number case
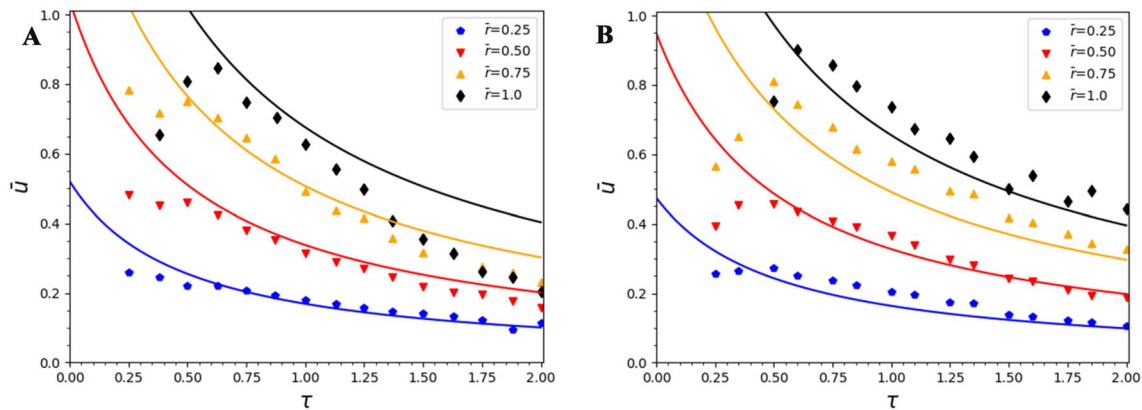

Fig. 15 Time evolution of non-dimensional radial velocity for different non-dimensional spreading radius **a** for moderate- and **b** high-Weber cases. Symbols represent the experimental data, while the solid curves represent Eq. (2)
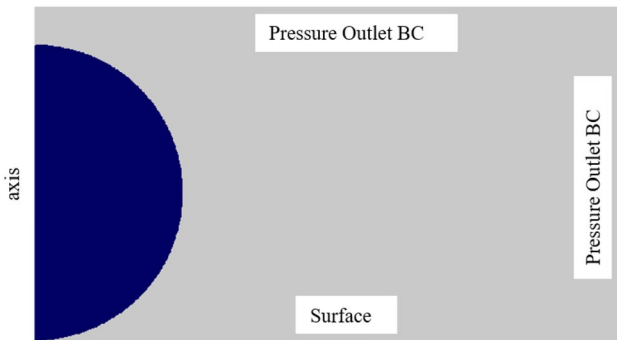

Fig. 16 Sketch of the computational domain and boundary conditions

surface temperatures of 200 °C and 250 °C, especially in later stages, increases the uncertainties in the radial velocities in external radial locations as severe disturbances are generated at the interface by the bubble nucleation. Moreover, the spreading velocities within the droplet pair are investigated at room temperature using the same methods. Another stagnation point due to the upward flow caused by the formation of the uprising sheet was observed in the interaction area. Afterwards, radial velocity measurements within the liquid lamellas were compared with an analytical model (Roisman et al. 2002) and a computational simulation for unheated surface temperature. For
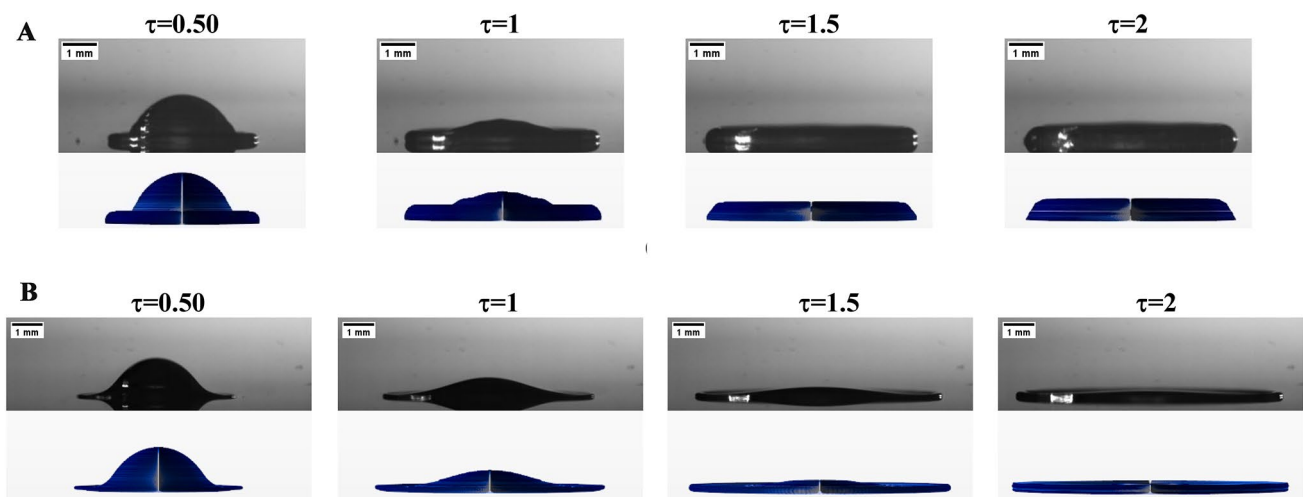
Fig. 17 Comparison between shadowgraph and computational images obtained for **a** moderate and **b** high *We* number cases

high-Weber number case, the analytical model largely agrees with the linear parts of the radial velocity profiles in the internal radial positions. For moderate Weber number case, the predicted radial velocity profile only agrees well with the linear parts of experimental data during early spreading process, but the inconsistency between the analytical model and PIV results rises in the later spreading and receding phases. Computational simulations are carried out using Star-CCM + and the volume of fluid model is used for interface tracking. Comparing the PIV results obtained with the computational simulations shows that there is a good agreement for both linear and non-linear parts in radial velocity profiles.
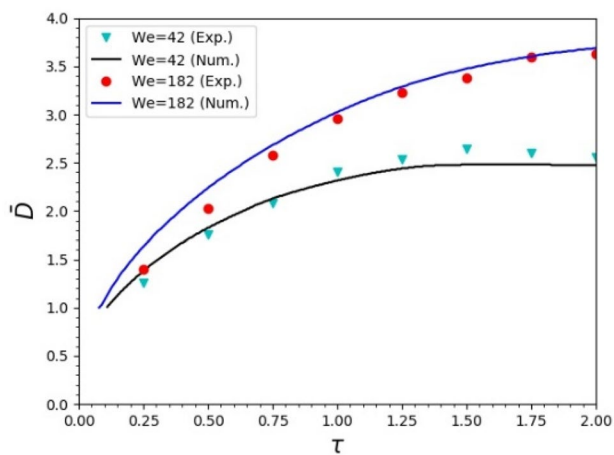
Fig. 18 Comparison between experimental and computational results for the non-dimensional spreading diameters with time
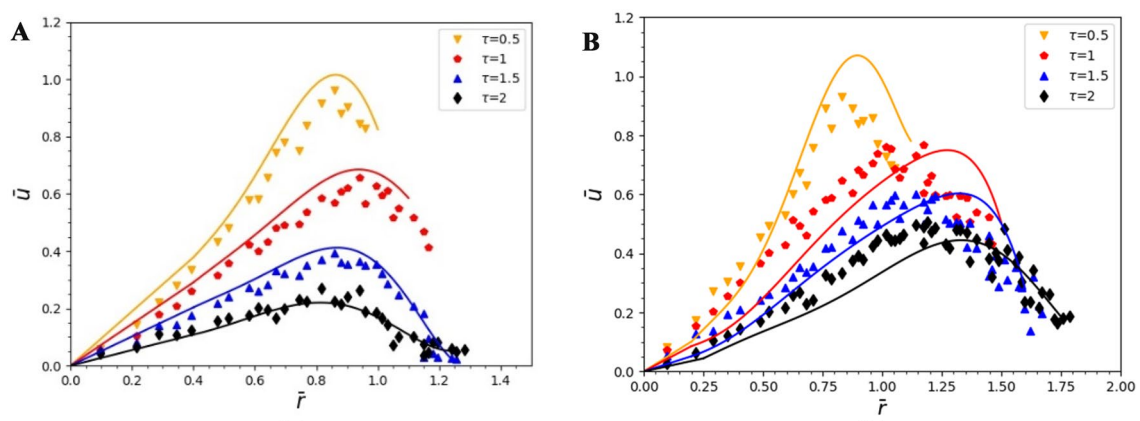

Fig. 19 Radial velocity profiles at room temperature for **a** moderate and **b** high *We* number cases. Symbols represent the PIV results, while the solid curves represent the computational results

Compliance with ethical standards

Conflict of interest The authors declare no conflict of interest.

References

Aarts DGAL, Lekkerkerker HNW, Guo H et al (2005) Hydrodynamics of droplet coalescence. Phys Rev Lett https://doi.org/10.1103/PhysRevLett.95.164503

Adrian RJ (2005) Twenty years of particle image velocimetry. Exp Fluids 39:159–169. https://doi.org/10.1007/s00348-005-0991-7

Al-Sharafi A, Yilbas BS (2019) Thermal and flow analysis of a droplet heating by multi-walls. Int J Therm Sci 138:247–262. https://doi.org/10.1016/j.ijthermalsci.2018.12.048

An S, Kim YI, Lee MW et al (2017) Wetting and coalescence of drops of self-healing agents on.pdf. Langmuir 33:10663–10672. https://doi.org/10.1021/acs.langmuir.7b02950

Brackbill JU, Kothe DB, Zemach C (1992) A continuum method for modeling surface tension. J Comput Phys 100:335–354. https://doi.org/10.1016/0021-9991(92)90240-Y

Cheng WL, Zhang WW, Chen H, Hu L (2016) Spray cooling and flash evaporation cooling: the current development and application. Renew Sustain Energy Rev 55:614–628. https://doi.org/10.1016/j.rser.2015.11.014

Cossali GE, Marengo M, Santini M (2003) Multiple drop impact on heated surface. In: Proceedings of the 9th international conference liquid atom and spray systems (ICLASS), Sorrento, Italy

de Gans B-J, Duineveld PC, Schubert US (2004) Inkjet printing of polymers: state of the art and future developments. Adv Mater 16:203–213. https://doi.org/10.1002/adma.200300385

Erkan N (2019) Full-field spreading velocity measurement inside droplets impinging on a dry solid-heated surface. Exp Fluids 60:1–17. https://doi.org/10.1007/s00348-019-2735-0

Erkan N (2016) Spreading velocities inside water droplets impinging on unheated and heated surfaces. At Sprays 26:799–814. https://doi.org/10.1615/AtomizSpr.2015014189

Erkan N, Okamoto K (2014) Full-field spreading velocity measurement inside droplets impinging on a dry solid surface. Exp Fluids. https://doi.org/10.1007/s00348-014-1845-y

Erkan N, Shinohara K, Someya S, Okamoto K (2008) Three-component velocity measurement in microscale flows using time-resolved PIV. Meas Sci Technol 19:057003. https://doi.org/10.1088/0957-0233/19/5/057003

Ersoy NE, Eslamian M (2020) Central uprising sheet in simultaneous and near-simultaneous impact of two high kinetic energy droplets onto dry surface and thin liquid film. Phys Fluids doi 10(1063/1):5135029

Eslamian M, Soltani-kordshuli F (2017) Development of multiple-droplet drop-casting method for the fabrication of coatings and thin solid film. J Coatings Technol Res 15:271–280. https://doi.org/10.1007/s11998-017-9975-9

Frommhold PE, Mettin R, Ohl CD (2015) Height-resolved velocity measurement of the boundary flow during liquid impact on dry and wetted solid substrates. Exp Fluids . https://doi.org/10.1007/s00348-015-1944-4

He M, Qiu H (2016) Internal flow patterns of an evaporating multicomponent droplet on a flat surface. Int J Therm Sci 100:10–19. https://doi.org/10.1016/j.ijthermalsci.2015.09.006

Hirt CW, Nichols BD (1981) Volume of fluid (VOF) method for the dynamics of free boundaries. J Comput Phys 39:201–225. https://doi.org/10.1016/0021-9991(81)90145-5

Jung J, Jeong S, Kim H (2016) Investigation of single-droplet/wall collision heat transfer characteristics using infrared thermometry. Int J Heat Mass Transf 92:774–783. https://doi.org/10.1016/j.ijheatmasstransfer.2015.09.050

Kang KH, Lim HC, Lee HW, Lee SJ (2013) Evaporation-induced saline Rayleigh convection inside a colloidal droplet. Phys Fluids. https://doi.org/10.1063/1.4797497

Karlsson L, Lycksam H, Ljung AL et al (2019) Experimental study of the internal flow in freezing water droplets on a cold surface. Exp Fluids 60:1–10. https://doi.org/10.1007/s00348-019-2823-1

Kim J (2007) Spray cooling heat transfer: the state of the art. Int J Heat Fluid Flow 28:753–767. https://doi.org/10.1016/j.ijheatfluidflow.2006.09.003

Lastakowski H, Boyer F, Biance A et al (2014) Bridging local to global dynamics of drop impact onto solid substrates. J Fluid Mech. https://doi.org/10.1017/jfm.2014.108

Lee MW, Kang DK, Yoon SS, Yarin AL (2012) Coalescence of two drops on partially wettable substrates. Langmuir 28:3791–3798. https://doi.org/10.1021/la204867c

Lee MW, Kim NY, Chandra S, Yoon SS (2013) Coalescence of sessile droplets of varying viscosities for line printing. Int J Multiph Flow 56:138–148. https://doi.org/10.1016/j.ijmultiphaseflow.2013.06.004

Liang G, Mudawar I (2017) Review of drop impact on heated walls. Int J Heat Mass Transf 106:103–126. https://doi.org/10.1016/j.ijheatmasstransfer.2016.10.031

Liang G, Yu H, Chen L (2019) Interfacial phenomena in impact of droplet array on solid wall. Acta Mech. https://doi.org/10.1007/s00707-019-02542-4

Menchaca-Rocha A, Martinez-Davalos A, Nunez R et al (2001) Coalescence of liquid drops by surface tension. Phys Rev E. https://doi.org/10.1103/PhysRevE.63.046309

Morozov VS, Volkov RS, Misyura SY (2018) Visualizing the velocity inside a drop when a cold droplet falls on a sessile drop on a hotwall. Interfacial Phenom Heat Transf 6:209–218. https://doi.org/10.1615/InterfacPhenomHeatTransfer.2018026188

Narhe RD, Beysens DA, Pomeau Y (2008) Dynamic drying in the early-stage coalescence of droplets sitting on a plate. A Lett J Explor Front Phys. https://doi.org/10.1209/0295-5075/81/46002

Panão MRO, Moreira ALN (2005) Flow characteristics of spray impingement in PFI injection systems. Exp Fluids 39:364–374. https://doi.org/10.1007/s00348-005-0996-2

Rioboo R, Marengo M, Tropea C (2002) Time evolution of liquid drop impact onto solid, dry surfaces. Exp Fluids 33:112–124. https://doi.org/10.1007/s00348-002-0431-x

Ristenpart WD, McCalla PM, Roy RV, Stone HA (2006) Coalescence of spreading droplets on a wettable substrate. Phys Rev Lett. https://doi.org/10.1103/PhysRevLett.97.064501

Roisman IV, Rioboo R, Tropea C (2002) Normal impact of a liquid drop on a dry surface: Model for spreading and receding. Proc R Soc A Math Phys Eng Sci 458:1411–1430. https://doi.org/10.1098/rspa.2001.0923

Roisman IV, Tropea C (2002) Multiple drop impact onto a dry solid substrate. J Colloid Interface Sci 410:396–410. https://doi.org/10.1006/jcis.2002.8683

Sahu RP, Sinha-Ray S, Yarin AL, Pourdeyhimi B (2012) Drop impacts on electrospun nanofiber membranes. Soft Matter 8:3957–3970. https://doi.org/10.1039/C2SM06744G

Sakai M, Hashimoto A, Yoshida N et al (2007) Image analysis system for evaluating sliding behavior of a liquid droplet on a hydrophobic surface. Rev Sci Instrum. https://doi.org/10.1063/1.2716005

Schneider CA, Rasband WS, Eliceiri KW (2012) NIH Image to ImageJ: 25 years of image analysis. Nat Methods 9:671–675. https://doi.org/10.1038/nmeth.2089

Sinha-Ray S, Zhang Y, Yarin AL (2011) Thorny devil nano-textured fibers: The way to cooling rates on the order of 1 kW/cm2. Langmuir 27:215–226. https://doi.org/10.1021/la104024t

Smith MI, Bertola V (2011) Particle velocimetry inside Newtonian and non-Newtonian droplets impacting a hydrophobic surface. Exp Fluids 50:1385–1391. https://doi.org/10.1007/s00348-010-0998-6

Yarin AL (2006) Drop Impact Dynamics : Splashing, Spreading, Receding, Bouncing. Annu Rev Fluid Mech. https://doi.org/10.1146/annurev.fluid.38.050304.092144

Yarin AL, Weiss DA (1995) Impact of drops on solid surfaces: self-similar capillary waves, and splashing as a new type of kinematic discontinuity. J Fluid Mech 283:141–173. https://doi.org/10.1017/S0022112095002266

Zhang Z, Li J, Jiang PX (2013) Experimental investigation of spray cooling on flat and enhanced surfaces. Appl Therm Eng 51:102–111. https://doi.org/10.1016/j.applthermaleng.2012.08.057

Affiliations

Ahmet Gultekin[1,2] (ID) **· Nejdet Erkan[2] · Uner Colak[1] · Shunichi Suzuki[2]**

[1] Energy Institute, Istanbul Technical University, 34469 Istanbul, Turkey

[2] Department of Nuclear Engineering and Management, The University of Tokyo, Tokyo, Japan